Photocatalytic chloride to chlorine conversion by ionic iron in aqueous aerosols: A combined experimental, quantum chemical and chemical equilibrium model study

Marie Kathrine Mikkelsen[1], Jesper Baldtzer Liisberg[1], Maarten M. J. W. van Herpen[2], Kurt V. Mikkelsen[1], and Matthew S. Johnson[1]

[1]Department of Chemistry, H. C. Ørsted Institute, University of Copenhagen, Universitetsparken 5, DK-2100 Copenhagen Ø, Denmark

[2]Acacia Impact Innovation, Maarten van Herpen, Bernheze 5384 BB, The Netherlands;

Correspondence: Matthew S. Johnson (msj@chem.ku.dk)

Abstract.

Prior aerosol chamber experiments show that the ligand-to-metal charge transfer absorption in iron(III) chlorides can lead to the production of chlorine (Cl_2/Cl). Based on this mechanism, the photocatalytic oxidation of chloride (Cl^-) in mineral dust-sea spray aerosols was recently shown to be the largest source of chlorine over the North Atlantic. However, there has not been a detailed analysis of the mechanism including the aqueous formation equilibria and the absorption spectra of the iron chlorides; neither has there been an analysis of which iron chloride is the main chromophore. Here we present the results of experiments measuring the photolysis of $FeCl_3 \cdot 6H_2O$ in specific wavelength bands, an analysis of the absorption spectra of $FeCl_n^{3-n}$ (n = 1 .. 4) made using density functional theory, and the results of an aqueous phase model that predicts the abundance of the iron chlorides with changes in pH and iron concentrations. Transition state analysis is used to determine the energy thresholds of the dissociations of the species. Based on a speciation model with conditions extending from dilute water droplet to acidic seawater droplet to brine to salty crust, and the absorption rates and dissociation thresholds, we find that $FeCl_2^+$ is the most important species for chlorine production for a wide range of conditions. The mechanism was found to be active in the range of 400 to 530 nm with a maximum around 440 nm. We conclude that iron chlorides will form in atmospheric aerosols from the combination of iron(III) cations with chloride and that they will be activated by sunlight, generating chlorine (Cl_2/Cl) from chloride (Cl^-), in a process that is catalytic in both chlorine and iron.

1 Introduction

Common components of atmospheric mineral dust including TiO_2 and Fe_2O_3 are photocatalytically active (Ponczek and George, 2018) and yet evidence of this playing a meaningful role in the atmospheric radical budget has been elusive (Abou-Ghanem et al., 2020; Chen et al., 2012). Recently, a large new source of chlorine atoms was discovered resulting from the combination of Sahara dust with sea spray aerosol over the North Atlantic (van Herpen et al., 2023). The mechanism is triggered when Sahara dust mixes with sea spray aerosol in the marine boundary layer. Iron from the Sahara dust is released and

forms iron chlorides with chloride from the sea spray. Iron chlorides can absorb sunlight, releasing a chlorine atom. The chlorine is emitted from the aerosol as molecular chlorine (Cl_2), which is then photolysed by sunlight to yield atomic Cl in the gas phase (Wittmer et al., 2015, 2016; Wittmer and Zetzsch, 2017). The chlorine produced by mineral dust-sea spray aerosols is estimated to produce 41 % of the chlorine over the Atlantic, impacting methane directly (Cl + CH_4) and indirectly (reduction in [O_3] from Cl + O_3 reduces OH source). Oeste proposed a method for intentionally increasing the production of chlorine using iron salt aerosol to achieve atmospheric methane removal (AMR) (Oeste, 2009; Meyer-Oeste, 2014). The use of chlorine from any source as a climate intervention was recently evaluated by Li et al. (2023).

Traditionally, the tropospheric chlorine cycle (Saiz-Lopez and von Glasow, 2012; Simpson et al., 2015) begins with the formation of sea spray aerosol (Nielsen and Bilde, 2020), which are known to be particles with high acidity (Angle et al., 2021). Acids such as HNO_3 and H_2SO_4 deposit forcing HCl into the gas phase which can react with OH to produce chlorine atoms, HCl + OH $\rightarrow$ Cl + H_2O (Young et al., 2014). Cl reacts with ozone, impacting the formation of hydroxyl radicals, and it reacts with methane and other hydrocarbons, reforming HCl (Chang and Allen, 2006; Knipping and Dabdub, 2003; Badia et al., 2019).

Chlorine production is poorly constrained and as a result, Cl is estimated to remove between 0.8 and 3.3 % of tropospheric methane, depending on the model (Allan et al., 2007; Hossaini et al., 2016; Sherwen et al., 2016; Gromov et al., 2018; Li et al., 2022). Multiple lines of evidence show chlorine concentrations in the troposphere exceed what can be explained with existing mechanisms. These include 1. ^{13}C depletion in CO in air samples from Barbados (Mak et al., 2003), a signature of methane oxidation by chlorine. 2. Anomalies in the CO:ethane ratio seen at Cape Verde (Read et al., 2009). 3. Observations of elevations in the concentration of HOCl above what can be explained with standard chemistry (Lawler et al., 2011). 4. A comprehensive simulation of tropospheric chlorine using the GEOS-Chem global 3-D model of oxidant–aerosol–halogen atmospheric chemistry could not explain the elevated Cl_2 mixing ratios measured in the boundary layer in the WINTER aircraft campaign (Wang et al., 2019).

Additional chlorine production impacts our understanding of the methane budget because the abundance of ^{13}C in atmospheric methane is used to constrain emissions sources, and because Cl + CH_4 has a large kinetic isotope effect, while the main atmospheric methane sink reaction OH + CH_4 does not. The reaction of CH_4 with Cl has a carbon kinetic isotope effect (KIE) of $^{13C}\text{KIE}_{Cl}$ = 1.066 ($\pm$0.002) at 297 K, which is around 17 times more fractionating than methane oxidation with OH radicals (Saueressig et al., 2001; Cantrell et al., 1990; Saueressig et al., 1995). The discovery of a new chlorine source means that methane sources must be more depleted than had been recognized, leading to the conclusion that previous methane emissions budgets, which did not include the new chlorine source, likely underestimate biogenic methane (e.g. wetlands and agriculture), and overestimate the fossil fuel source (van Herpen et al., 2023). To understand the methane budget it is imperative to fully characterize the chlorine production mechanism and to see how it will vary with chemical conditions such as pH, chloride concentration and the concentrations of possibly interfering ions.

Historically, iron(III) chloride has been believed to form four complexes: $FeCl^{2+}$, $FeCl_2^+$, $FeCl_3$, and $FeCl_4^-$ (Gamlen and Jordan, 1953). Uchikoshi et al. (2022) presented a model of iron(III) chloride species, which shows the most plausible species to be $FeCl_2^+$, $FeCl_3$, $FeCl_4^-$, and $FeCl_6^{3-}$. With the use of a theoretical mathematical decomposition model called the "Multivariate

Curve Resolution Alternative Least Squares (MCRALS)" and a "5 complex model", they determined that the combination of Cl coordination numbers are $n = 0$, 2, 3, 4, and 6. That study indicates that $FeCl^{2+}$ will not be formed and the highest chlorinated complex, forming at the highest chloride concentrations, will be $FeCl_6^{3-}$. The research by Uchikoshi et al. (2022) shows $FeCl_2^+$, $FeCl_3$, and $FeCl_4^-$ forming at a lower chloride concentration than previously expected. However, $FeCl_6^{3-}$ has not been implemented in this study.

In this study, we present a detailed description of the photocatalytic oxidation of chloride to chlorine-based on four iron(III) chloride complexes: $FeCl^{2+}$, $FeCl_2^+$, $FeCl_3$, and $FeCl_4^-$. A combination of modelling, quantum chemical calculations and laboratory experiments explains the formation constants of the iron chlorides under changing conditions of pH and chloride concentration, their absorption rates under tropospheric sunlight, the quantum yield of absorption resulting from the energy threshold for photodissociation to yield a Cl radical, and the production of Cl_2 from irradiation of $FeCl_3 \cdot 6H_2O$.

1.1 The Fe(III)Cl_n^{3-n} system

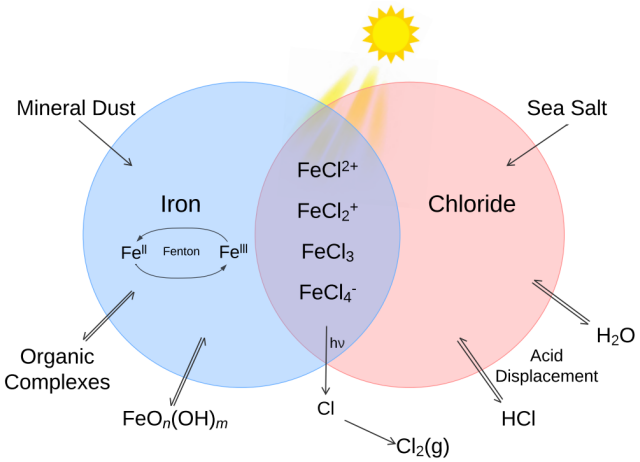

Figure 1. The primary sources and sinks for iron(II) and iron(III) ions and chloride in the atmospheric aerosols and their influence on the formation of iron(III) chlorides in a low pH environment.

Various Fe(III) complexes form in marine boundary layer aerosol, where the speciation depends on pH, salt composition, chloride concentration, water activity and ionic strength. The Pourbaix diagram of aqueous iron shows that dissolved iron will be in the form of free Fe(III) and not $Fe(OH)_3$, Fe(II) or $Fe(OH)_2$ given acidic and oxidising conditions (pH<3.6 and E_H>0.72 V) (Harnung and Johnson, 2012). Given the presence of chloride and Fe(III), the iron(III) chlorides will form.

The central Fe(III)Cl_n^{3-n} reactions that occur in an aerosol or the marine boundary layer are shown in Reaction R1 for n=0..3 (Lindén et al., 1993).

$$FeCl_n^{3-n} + Cl^- \rightleftharpoons FeCl_{n+1}^{2-n} \quad \text{(R1)}$$

Iron(III) chloride formation may be inhibited by the presence of other ions such as sulfate or fluoride, or by organic compounds such as oxalate that bind with Fe(III).

The photolysis of the iron(III) chlorides is shown in general form in Reaction R2 for $n \geq 1$. In this ligand to metal electron transfer absorption Fe(III) is reduced to Fe(II) and chloride is oxidised yielding a chlorine atom (Lindén et al., 1993; Nadtochenko and Kiwi, 1998).

$$\mathrm{FeCl}_n^{3-n} + h\nu \quad \rightarrow \quad \mathrm{FeCl}_{n-1}^{3-n} + \mathrm{Cl}\cdot \tag{R2}$$

For example for n =1, reaction R2 has a quantum yield of 0.5 ± 0.1 at a wavelength of 347 nm. At higher pH the formation of iron(III) chloride complexes competes with iron hydroxide complexes (also depending on [Cl^-]), Reaction R3 and R4.

$$\mathrm{Fe^{3+}} + \mathrm{OH^-} \quad \rightleftharpoons \quad \mathrm{FeOH^{2+}} \tag{R3}$$

$$\mathrm{FeOH^{2+}} + \mathrm{OH^-} \quad \rightleftharpoons \quad \mathrm{Fe(OH)_2^+} \tag{R4}$$

Iron(III) hydroxide complexes can be photolysed, similar to iron(III) chlorides, however only some of the iron is photoreduced; Reaction R5 produces OH radicals with a quantum yield of 0.21 ± 0.04 at a wavelength of 347 nm (Nadtochenko and Kiwi, 1998). Where reaction R6 shows the photolysis of $Fe(OH)_2^+$ does not grant a reduction of iron (Loures et al., 2013; Korte et al., 2011).

$$\mathrm{Fe(OH)^{2+}} + h\nu \quad \rightarrow \quad \mathrm{Fe^{2+}} + \mathrm{OH^{\cdot}} \tag{R5}$$

$$\mathrm{Fe(OH)_2^+} + h\nu \quad \rightarrow \quad \mathrm{FeOH^{2+}} + \mathrm{OH^-} \tag{R6}$$

In the aerosol process, the Fe(II) product is oxidised back to Fe(III) by one half of the Fenton process. In one example, for marine mineral aerosol, Zhu et al. found the oxidation rate to be 0.19 min^{-1} (Zhu et al., 1993). The Fenton process describes how Fe(II) and Fe(III) act as a catalyst pair, breaking down hydrogen peroxide and generating radicals (Fenton, 1894). The Fenton reactions are shown in Reactions R7 to R9. Hydroxyl may react or escape to the gas phase.

$$\mathrm{Fe^{2+}} + \mathrm{H_2O_2} \quad \rightarrow \quad \mathrm{Fe^{3+}} + \mathrm{OH}\cdot + \mathrm{OH^-} \tag{R7}$$

$$\mathrm{Fe^{3+}} + \mathrm{H_2O_2} \quad \rightarrow \quad \mathrm{Fe^{2+}} + \mathrm{HO_2}\cdot + \mathrm{H^+} \tag{R8}$$

$$\text{Net}: 2H_2O_2 \quad \rightarrow \quad OH\cdot + HO_2\cdot + H_2O \tag{R9}$$

Wittmer and Zetzsch (2017) proposed that the production of OH will enhance Cl_2 production due to the production of a chlorine radical, shown in reactions R10 to R12. This route could be enhanced in chloride-rich environments. Several sources of OH are known including photocatalytic minerals (Chen et al., 2012) and Fenton degradation of H_2O_2 reaction R7.

$$OH^{\cdot} + Cl^- \quad \rightarrow \quad ClOH^{\cdot -} \tag{R10}$$

$$ClOH^{\cdot -} + H^+ \quad \rightarrow \quad ClOH_2^{\cdot} \tag{R11}$$

$$ClOH_2^{\cdot} \quad \rightarrow \quad Cl\cdot + H_2O \tag{R12}$$

Reactions R10 to R12 take place in the aqueous phase. For the chloride produced in Reaction R2 and the chlorine radical in R12 to impact gas phase chemistry, it must escape the particle. The following Reactions, R13 and R14, lead to the production of Cl_2(aq) in Reaction R15.

$$Cl^- + Cl\cdot \quad \rightleftharpoons \quad Cl_2^- \tag{R13}$$

$$2Cl_2^- \quad \rightleftharpoons \quad Cl_2 + 2Cl^- \tag{R14}$$

$$Cl_2^- + Cl\cdot \quad \rightleftharpoons \quad Cl_2 + Cl^- \tag{R15}$$

Chlorine atoms may be lost before escaping as molecular chlorine in the gas phase. Possible mechanisms include failure of the chlorine atom produced by photolysis to escape the solvent cage or diffusion back into contact leading to reformation of the iron chloride, and reaction of chlorine with condensed phase hydrocarbons forming HCl/Cl^-.

Once in gas phase, molecular chlorine is activated by light, shown in Reaction R16. Cl_2(g) absorbs in a band centred at 330 nm (Maric et al., 1993).

$$Cl_2(g) + h\nu \quad \rightarrow \quad 2Cl\cdot(g) \tag{R16}$$

Table 1. Species and initial concentrations listed for each AEM scenario. Two different iron concentrations are used for each: iron seawater concentration, marked S and iron aerosol concentration, marked A.

Aqueous Equilibrium Model (AEM)			
Models:	Simple	Sulphate	Seawater
Species	Concentration / mol/kg		
Total Fe $_S^{(a)}$	9.76×10^{-13}	9.76×10^{-13}	9.76×10^{-13}
Fe_S^{2+} $^{(b)}$	7.32×10^{-14}	7.32×10^{-14}	7.32×10^{-14}
Fe_S^{3+} $^{(b)}$	9.02×10^{-13}	9.02×10^{-13}	9.02×10^{-13}
Total Fe $_A^{(c)}$	9.17×10^{-4}	9.17×10^{-4}	9.17×10^{-4}
Fe_A^{2+} $^{(b)}$	6.88×10^{-5}	6.88×10^{-5}	6.88×10^{-5}
Fe_A^{3+} $^{(b)}$	8.48×10^{-4}	8.48×10^{-4}	8.48×10^{-4}
H^+ $^{(d)}$	0	0	0
Cl^-	5.47×10^{-1}	5.47×10^{-1}	5.47×10^{-1}
Na^+	4.69×10^{-1}	4.69×10^{-1}	4.69×10^{-1}
SO_4^{2-}		2.82×10^{-2}	2.82×10^{-2}
Mg^{2+}			5.24×10^{-2}
Ca^{2+}			1.03×10^{-2}
K^+			1.02×10^{-2}
Sr^{2+}			9.12×10^{-5}
HCO_3^-			2.33×10^{-3}
Br^-			8.54×10^{-4}
F^-			6.79×10^{-5}
B			4.13×10^{-4}
H_4SiO_4 $^{(e)}$			3×10^{-5}

$^{(a)}$ The mean value of the total iron concentration in seawater was obtained from Achterberg et al. (2001). $^{(b)}$ Ratio of Fe^{2+} and Fe^{3+} is 7.5% and 92.5% respectively, from Zhu et al. (1993). $^{(c)}$ The total iron concentration in aerosols obtained from Hsu et al. (2010). $^{(d)}$ Required species for the AEM. $^{(e)}$ Value obtained from Harnung and Johnson (2012). Concentrations for unmarked species are found in Stumm and Morgan (2012).

2 Methods

This section will include method details of the study divided into three main parts: Aqueous Equilibrium Model (AEM) (modelling the concentrations of $FeCl_n^{3-n}$ species), Ab Initio Calculations (estimating absorption rates), and Laboratory Experiments (prove the formation of chloride from photolysis of $FeCl_n^{3-n}$ species).

2.1 Aqueous Equilibrium Model Methods

Visual MinteQ is a chemical equilibrium model that calculates the equilibrium speciation for the input species and predicts their concentration (J. P. Gustafsson, (released 2014). The program has been used to evaluate species with direct or indirect effects on iron(III) induced chloride production.

Three AEM scenarios shown in Table 1, called Simple, Sulphate, and Seawater. The species $FeCl^{2+}$, $FeCl_2^+$, and $FeCl_3$ were manually added to the database, shown in the Appendix Table A1 (Tagirov et al., 2000), however, $FeCl_4^-$ could not be added because the thermodynamic data is not available. Two different iron concentrations correlating to seawater and aerosol concentrations are used in all models, where the ratio between Fe^{2+} and Fe^{3+} is estimated to be 7.5 to 92.5 $\%$ (Achterberg et al., 2001; Hsu et al., 2010; Zhu et al., 1993). The Simple model shows the relation between iron chloride species, the Sulphate model evaluates the potential effect of SO_4^{2-} on iron chlorides, and the Seawater model includes all major ions found in seawater (Harnung and Johnson, 2012; Stumm and Morgan, 2012). The results from each of the three models are shown as species concentrations and iron species as a fraction of total iron, as a function of pH in Section 3.1.

2.2 Ab Initio Calculations

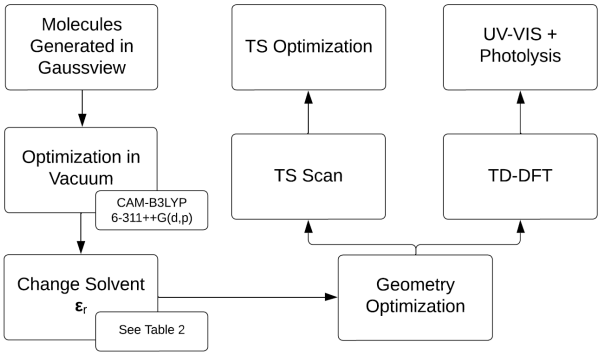

Figure 2. Overview of the computational strategy, highlighting key components: the relative permittivity (ϵ_r), transition state (TS), and time-dependent density functional theory (TD-DFT).

Figure 2 describes the computational method, initialized by the generation of the molecules in Gaussview followed by geometry optimizations in vacuum (Frisch et al., 2016). The density functional theory method CAM-B3LYP/6-311++G(d,p) was used for all calculations (Yanai et al., 2004; Francl et al., 1982; McLean and Chandler, 1980; Spitznagel et al., 1987). Solvents were modelled using the PCM model (Tomasi et al., 1999). The relative permittivity, ϵ_r, for the solvents is in Table 2. See Appendix A2 for the geometries of the iron(III) chlorides.

A transition state scan was made to evaluate the bond dissociation energy. In a few cases (mainly $FeCl_4^-$) in some solvents, the TS optimizations did not converge. TD-DFT calculations were used to explore the excitation energies of the molecules. Photolysis rates j_A were calculated using Equation 1.

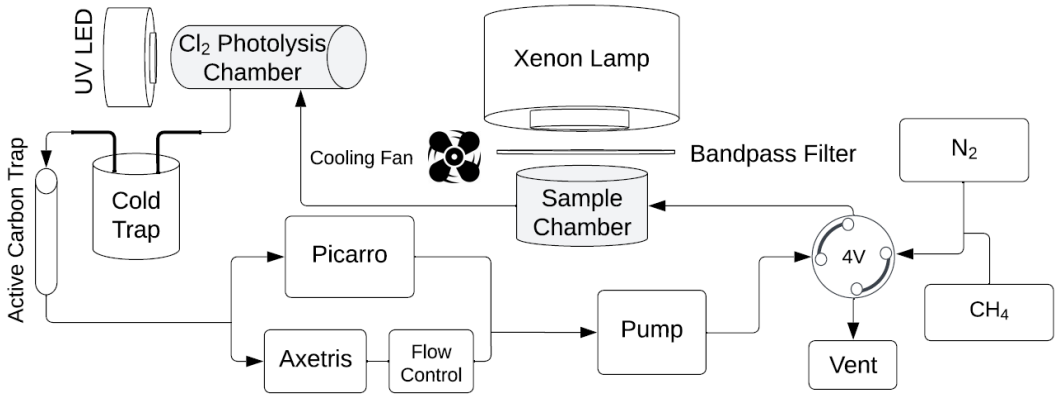

Figure 3. Overview of the system used in the laboratory experiments. The sample is located in "Sample Chamber". The volume of the "Sample Chamber" and "Cl_2 Photolysis Chamber" is 0.36 and 0.45 L, respectively. The four-port valve, "4V", changes the system between flow and loop mode.

Table 2. The set of relative permittivities (relative permittivity, ϵ_r) used to represent various solvents with the PCM model.

Solvent	ϵ_r
Water [a]	78.4
NaCl solutions [b]	78.3
	77.5
	77.3
	73.6
	68.3
Seawater [b]	69.0
Arbitrary investigation [c]	60.0
	50.0
	40.0
	30.0
	20.0
Solid $FeCl_3$, static [d]	10.0
Solid $FeCl_3$, optic [d]	2.0

[a] Value obtained from Gaussview, Frisch et al. (2016). [b] Values obtained from Midi et al. (2014). [c] Arbitrary values were only used for $FeCl_3$. [d] Estimations.

$$j_A = \int_{\lambda_1}^{\lambda_2} \phi_A(\lambda,T) \cdot \sigma_A(\lambda,T) \cdot I(\lambda) d\lambda \quad (1)$$

where the variables represent the molecular absorption cross-section, σ_A (cm^{-2}), spectral actinic flux, I (n_{hv} cm^2 s^{-1} nm^{-1}), and quantum yield, ϕ_A (set to 1) (Seinfeld and Pandis, 2008). The absorption cross-section was evaluated computationally, and the spectral actinic flux was determined using the TUV model for conditions corresponding to the Marine Boundary Layer in the Atlantic, west of Cape Verde (18.97°N, 39.12°W, date 18/07/2022, 12:00) (Madronich et al., 2002).

2.3 Experimental Method

The experimental system is shown in Figure 3. Gasses are introduced with a 4-port valve ("4V"), which was used to choose a flow-through or loop pattern. The average flow was measured to be 125 mL/min. A sample of $FeCl_3 \cdot 6H_2O$ was placed in the Sample Chamber (volume 0.36 L) illuminated by a Xenon lamp. For wavelength-controlled experiments, a bandpass filter is placed on top of the Sample Chamber. The "Cl_2 Photolysis Chamber" is a photolysis chamber with a volume of 0.45 L and a high-power UV LED light source, that ensures chlorine emitted by the sample in the Sample Chamber is photolysed. The cold trap and active carbon trap ensure that organic molecules and carbon dioxide are captured, which protects the instruments and removes possible interference. The airflow is divided for analysis by the Picarro "G2201-i Analyser for Isotopic CO_2/CH_4" and the Axetris "LGD Compact-A CH_4" which measure CH_4, $\delta^{13}CH_4$, CO_2, and H_2O. The flow controller is set to 125 mL/min and the pump ensures flow through the system.

At the beginning of every experiment, the active carbon trap and cold trap are flushed and a new sample of 20 mg $FeCl_3 \cdot 6H_2O$ in a 10 mL beaker is placed in a cleaned Sample Chamber. Methane is introduced to achieve a nominal mole fraction of 95 ppm and the system is switched to loop mode. The concentrations of methane and carbon dioxide are monitored and a leak test of the system is performed after the concentrations have stabilized. System stability is monitored for 10 minutes, the xenon lamp is turned on for 15 minutes, and finally, an additional 10 minutes of measurement are taken to verify system stability. The duration of an experiment is from 1.5 to 2.5 hours. Three repetitions were made for each bandpass filter. The experimental procedure is described in greater detail in Appendix Figure A1.

Two light sources were used: a Xenon lamp from Eimac, see Figure 4, and a UV-LED (Luminus SST-10-UV Surface Mount LED lamp) see Appendix Figure A2. The spectrum of the xenon lamp is shown with a dashed line in Figure 4; the light that enters the Sample Chamber is illustrated with a solid line. The legend name refers to the centre wavelength of the bandpass filter in nm. The system and measurements of the Sample Chamber, bandpass filters, and the xenon lamp are illustrated in Appendix Figure A3.

3 Results

The results are presented in three sections: Aqueous Equilibrium Modelling, Ab Initio Calculations, and Laboratory Experiments.

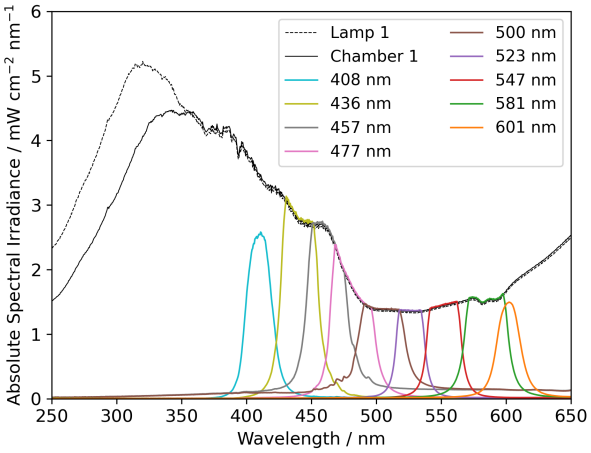

Figure 4. The measured absolute spectral irradiance of the xenon lamp before and after the Sample Chamber, including bandpass filters. Recorded with the Ocean Optics spectrometer.

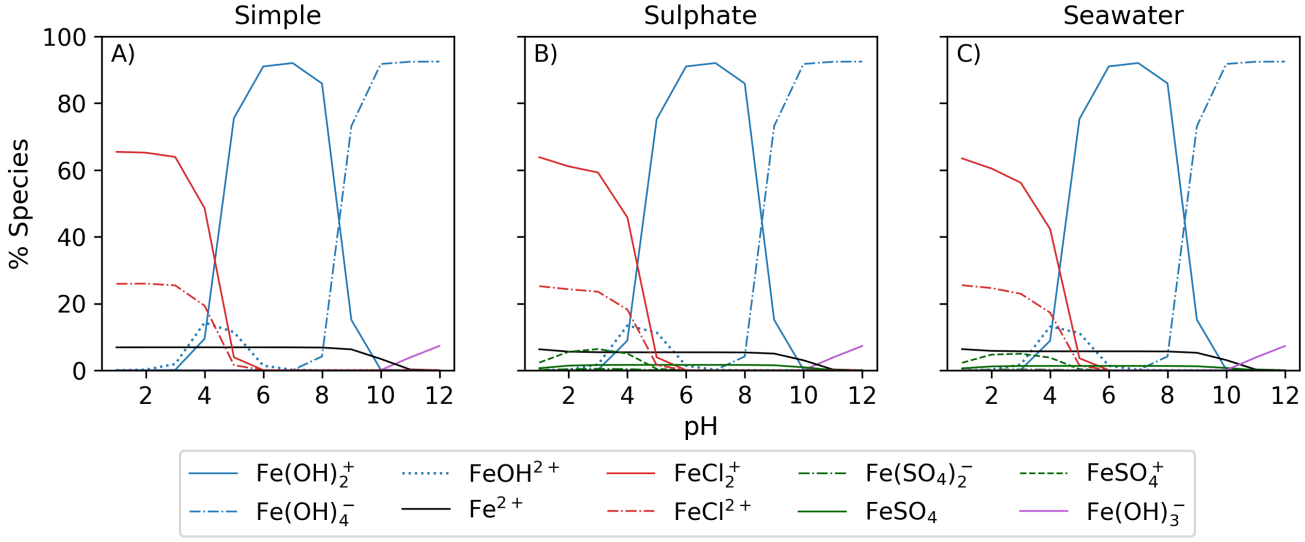

Figure 5. Three AEM scenarios with a seawater iron concentration of 9.76 $\times 10^{-13}$ mol/kg (Fe_S) at 20 °C. All species below 5 % are shown in Appendix B2. See Appendix B3 and B4 for AEM scenarios with increased sulphate and iron concentration, e.g. $Fe(OH)_3$.

3.1 Aqueous Equilibrium Modelling

Figure 5 displays the iron speciation from the three AEM scenarios as a function of pH for the seawater iron concentration of 9.76 $\times 10^{-13}$ mol/kg. Iron(III) chlorides are stable at pH values less than 4. Above this, the dominant species are iron

hydroxides. This trend is consistent for all models in Figure 5. According to the AEM scenarios, the two dominant iron(III) chloride species are $FeCl^{2+}$ and $FeCl_2^+$, both observed in a low pH environment. The Sulphate model, Figure 5B, shows a slight decrease of the iron(III) chloride concentrations in the same pH range as the iron sulfates. However, increasing the sulphate concentration by a factor of 10 shows that sulfate is able to block the availability of some iron to form iron chlorides, see Appendix Figure B3. In this scenario, Sulphate changes the iron(III) chloride concentration by up to 40 % compared to the Simple model. The seawater model, Figure 5C, does not show any major changes compared to the sulphate model. Moreover, this is consistent for the scenarios with increased sulphate and iron concentration shown in Appendix Figure B3 and B4. According to this study, sulphates are the main seawater anion, competing for iron(III) with chloride. Increasing the sulphate and iron concentration has a small impact on the speciation of iron fluorides as seen in Appendix section B2, where all species above 0.1 % for all models are shown. The fraction of iron fluorides is below 5 % and they will not be discussed further.

The temperature dependence of $FeCl^{2+}$ and $FeCl_2^+$ was modelled with the Seawater scenario of the AEM illustrated in Figure 6 from 0 to 100 °C. The fraction of $FeCl^{2+}$ increases with increasing temperature and the opposite trend is seen for $FeCl_2^+$. With varying temperatures, a change of 70 and 45 % is found for $FeCl^{2+}$ and $FeCl_2^+$, respectively. Thus, temperature is an important parameter when calculating the rate of chlorine production from iron chlorides, as a change of 20 °C will significantly change iron speciation.

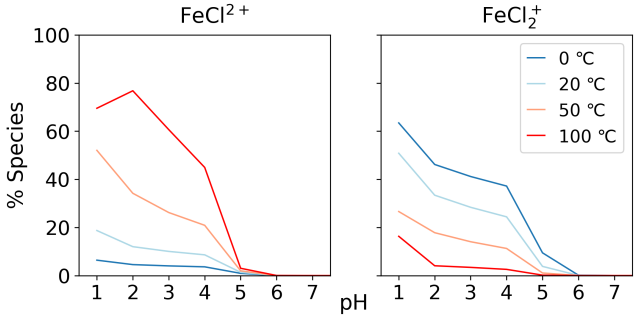

Figure 6. Temperature dependence of $FeCl^{2+}$ and $FeCl_2^+$ with seawater iron concentration of 9.76 $\times 10^{-13}$ mol/kg (Fe_S).

3.2 Ab Initio Calculations

The four species $FeCl^{2+}$, $FeCl_2^+$, $FeCl_3$ and $FeCl_4^-$ were investigated computationally with the DFT functional CAM-B3LYP and basis set 6-311++G(d,p) (Yanai et al., 2004; Francl et al., 1982; McLean and Chandler, 1980; Spitznagel et al., 1987). UV-Vis spectra were extracted from TD-DFT calculations done with a variety of relative permittivities, shown in Table 2. UV-Vis spectra for $FeCl_3$ are displayed in Appendix Figure B1, showing an increasing red shift with increasing dielectric constant. This relative permittivity effect means that the solvation of iron chlorides in water increases the absorption cross-section at longer wavelengths where there is higher actinic flux, increasing the photolysis rate. The absorption spectra obtained for relative

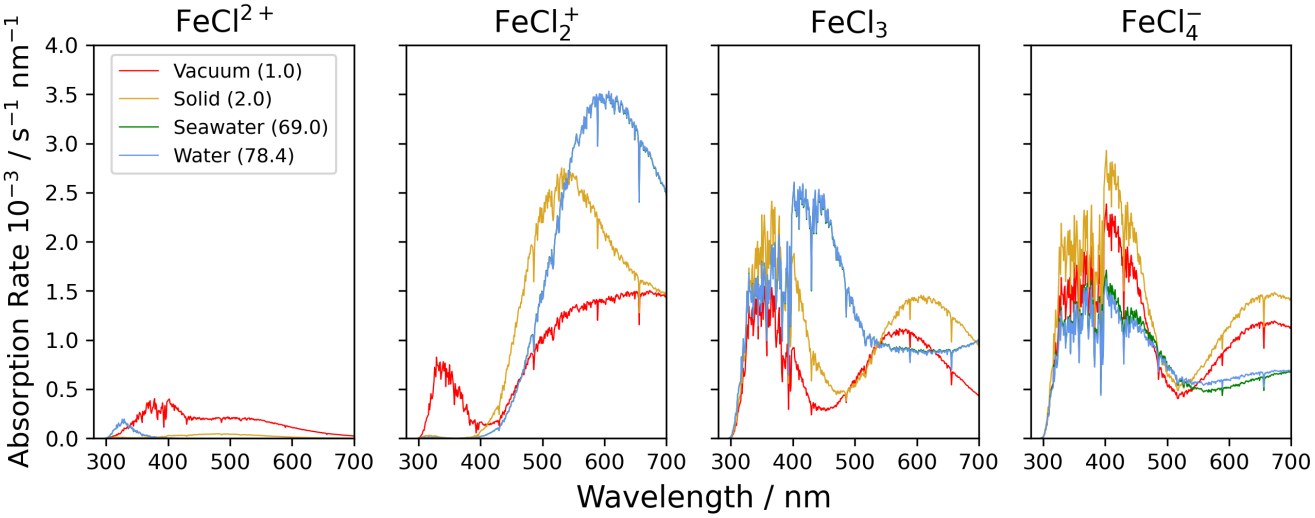

Figure 7. The absorption rate of $FeCl^{2+}$, $FeCl_2^+$, $FeCl_3$ and $FeCl_4^-$ in Vacuum (1.0), Solid $FeCl_3$ (2.0), Seawater (69.0), and Water (78.4). The value in parentheses shows the relative permittivity of the solute. The absorption is calculated using the CAM-B3LYP/6-311++G(d,p) basis set. The spectral actinic flux is calculated using the TUV model over the Atlantic Ocean, west of Cape Verde (18.97°N, 39.12°W, date 18/07/2022, 12:00) (Madronich et al., 2002).

permittivities greater than 2 are seen to be virtually identical, thus, only the four environments vacuum, solid, seawater, and water, are discussed further.

Using the calculated UV-Vis spectra, the actinic flux and the quantum yield function, the photolysis spectra of $FeCl^{2+}$, $FeCl_2^+$, $FeCl_3$, and $FeCl_4^-$ are calculated, see Figure 7. Each of these species absorb at visible wavelengths, which has not been described previously. The modelled result for Seawater (green) is almost identical to the result for water (blue); the two spectra overlap in the figure. The lowest absorption rates are calculated for $FeCl^{2+}$ where all rates are below 0.5×10^{-3} s^{-1} nm^{-1} for all four solvents. The AEM scenarios found $FeCl^{2+}$ to be the second most abundant iron(III) chloride species. Its role becomes less important however when the absorption spectrum is considered, in addition to the chromophore's concentration.

$FeCl_2^+$ in vacuum absorbs from 300 to 700 nm whereas solid, seawater, and aqueous $FeCl_2^+$ absorb in the range of 400 to 700 nm. $FeCl_2^+$ in water and seawater have the highest absorption rates of the investigated species, 3.5×10^{-3} s^{-1} nm^{-1}. The AEM scenarios found $FeCl_2^+$ to be the dominant iron(III) chloride species and when the absorption spectrum is considered in combination with concentration, we conclude that $FeCl_2^+$ is the important chromophore for the catalytic, photo-oxidative conversion of chloride to chlorine in aqueous environments.

In the model, the absorption rates of $FeCl_3$ in seawater and water have a maximum of 2.6×10^{-3} s^{-1} nm^{-1} at 402 nm. Similar trends are calculated for $FeCl_4^-$ where the solid has a maximum at 400 nm of 2.8×10^{-3} s^{-1} nm^{-1}. The absorptions in vacuum and solid have similar trends for both $FeCl_3$ and $FeCl_4^-$.

Visible light does not necessarily provide enough energy for the iron(III) chlorides to dissociate, and a transition state analysis can assist in the estimation of the energy thresholds. In Figure 8 the energy thresholds for photodissociation yielding a chlorine radical are shown for the four iron(III) chloride species $FeCl^{2+}$, $FeCl_2^+$, $FeCl_3$, and $FeCl_4^-$. The photon energy is given in kJ/mol and converted to a photon wavelength in nm so it can be related to the solar spectrum. Near the Earth's surface, the actinic flux spectrum becomes negligible at wavelengths shorter than 300 nm (Harnung and Johnson, 2012). This threshold is shown in the figure with a yellow line.

Figure 8 shows $FeCl^{2+}$ as the only species to have an energy threshold corresponding to a wavelength shorter than 300 nm for solid, seawater, and water and so this species can not be dissociated by near-surface solar excitation. According to the model, $FeCl_2^+$ has energy thresholds for solid, seawater, and water at 611, 603, and 605 nm, respectively. The highest absorption rates for $FeCl_2^+$ are in the region of 500 to 700 nm (see Figure 7), thus these thresholds very likely impact the photolysis rate.

According to the transition state model, $FeCl_3$ is the only species that can be photolysed by all visible wavelengths and even into the near-infrared, for any of the solvents. For $FeCl_4^-$ the only sunlight-limiting energy threshold is in vacuum, at 573 nm. However, as $FeCl_4^-$ absorbs at wavelengths shorter than this threshold, sunlight will dissociate this species under vacuum conditions. Sunlight at the surface has photons with enough energy for the dissociation of $FeCl_2^+$, $FeCl_3$, and $FeCl_4^-$.

General trends in Figure 8 show vacuum to be an outlier that either has a higher or lower energy threshold than solid, seawater, and water. Therefore, solvent effects play an important role when estimating the energy thresholds and absorption rates of the dissociation of these iron(III) chloride species.

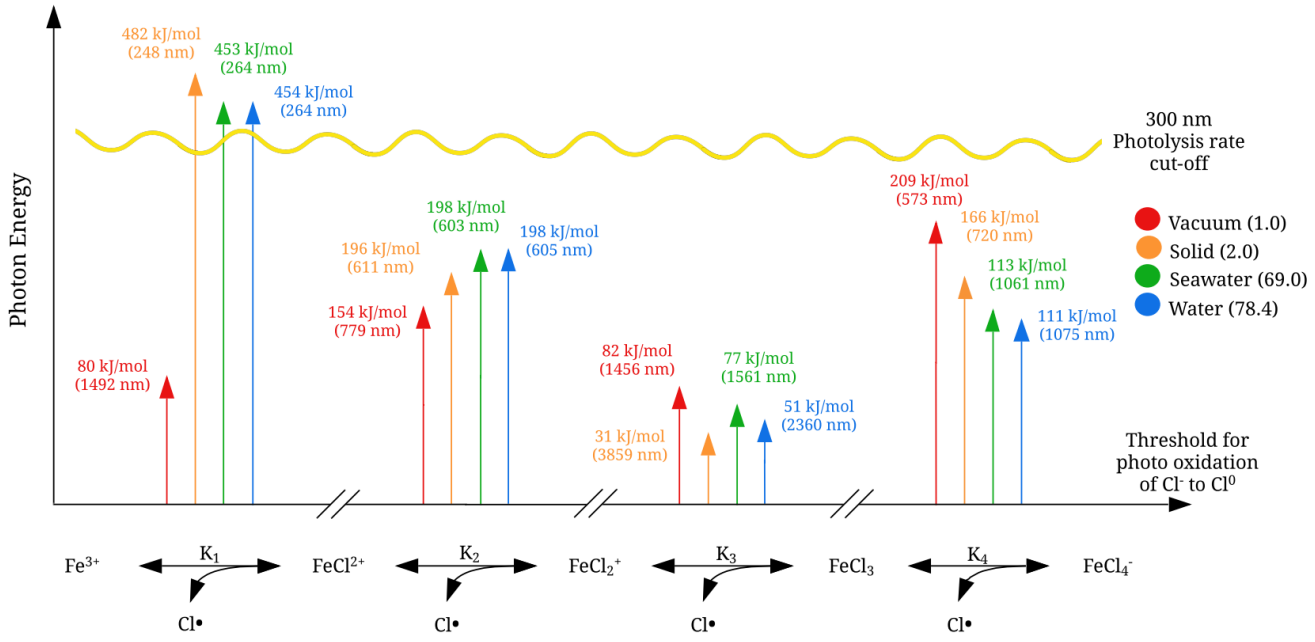

Figure 8. Energy thresholds for photodissociation, yielding a chlorine radical calculated with CAM-B3LYP/6-311++G(d,p). The sunlight photolysis rate cut-off is illustrated in yellow. The relative permittivity for the solutes is given in parentheses.

Table 3. Integrated Absorption Rates, $s^{-1} \times 10^{-3}$. "Full" is integrated from 280 to 700 nm, as displayed in Figure 7. "Cut-off" is integrated from 280 nm to the dissociation energy threshold in Figure 8. The deviation is calculated between the Full and the Cut-off absorption rates.

		$FeCl^{2+}$	**$FeCl_2^+$**	**$FeCl_3$**	**$FeCl_4^-$**
Vacuum	Full $\times 10^{-3}$ / s^{-1}	32	177	150	220
	Cut-off $\times 10^{-3}$ / s^{-1}	32	177	150	113
	Deviation / %	0	0	0	48
Solid	Full $\times 10^{-3}$ / s^{-1}	4	256	222	272
	Cut-off $\times 10^{-3}$ / s^{-1}	0	141	222	272
	Deviation / %	100	45	0	0
Seawater	Full $\times 10^{-3}$ / s^{-1}	3	312	259	164
	Cut-off $\times 10^{-3}$ / s^{-1}	0	131	259	164
	Deviation / %	100	58	0	0
Water	Full $\times 10^{-3}$ / s^{-1}	3	312	259	164
	Cut-off $\times 10^{-3}$ / s^{-1}	0	134	259	164
	Deviation / %	100	57	0	0

To relate the absorption rates and the energy dissociation threshold, the integrated absorption rates are listed in Table 3. The integrated absorption rate is integrated from 280 to 700 nm, as seen in Figure 7. The ”cut-off” is integrated from 280 nm to the dissociation energy threshold regarding each species, as seen in Figure 8. The deviation between ”Full” and ”Cut-off” is listed in percentages for each species as a measure of the cut-off impact.

As listed in Table 3, $FeCl^{2+}$ has full absorption rates of 32, 4, 3, and 3 s^{-1} in a vacuum, solid, seawater, and water, respectively. This species generally has the lowest integrated absorption rates which decrease significantly from vacuum to solid, seawater, and water. When the energy dissociation threshold is included, the integrated absorption rates for solid, seawater, and water decrease to zero.

$FeCl_2^+$ has full absorption rates of 177, 256, 312, and 312 s^{-1} in vacuum, solid, seawater, and water, respectively. Including the cut-off significantly decreases the absorption rates by 45, 58 and 57 % for solid, seawater and water, respectively.

$FeCl_3$ has full absorption rates of 150, 222, 259, and 259 s^{-1} in vacuum, solid, seawater, and water, respectively. $FeCl_3$ is the only species that does not have sunlight-limiting energy thresholds; hence, the full and cut-off rates are identical. Furthermore, $FeCl_3$ has a higher cut-off absorption rate for seawater and water than the other species, which increases the importance of this species.

$FeCl_4^-$ has full absorption rates of 220, 272, 164, and 164 s^{-1} in vacuum, solid, seawater, and water, respectively. The rates significantly decrease from vacuum to seawater and water. However, including the cut-off significantly decreases the rate in vacuum by 48 %, whereas the rate in water and seawater is unaffected and is consequently faster than the rate in vacuum.

Including the sunlight limiting energy thresholds, $FeCl_3$ is the species that has the fastest integrated absorption rates in seawater and water of 259 and 259 s^{-1}, respectively. Across all species, seawater and water have virtually identical rates, which further confirms that quantum calculations made in water can be used to evaluate behaviour in seawater.

3.3 Laboratory Study

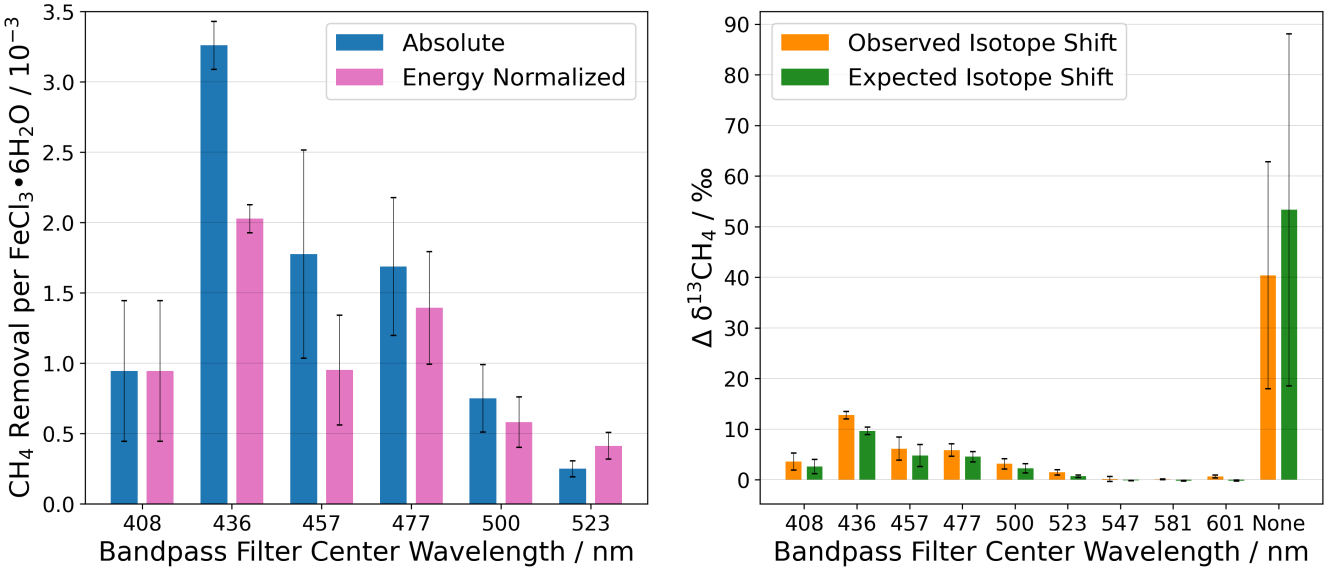

Figure 9. (Left) Chlorine generation measured as methane removal for photoexcitation in a series of wavelength intervals defined by bandpass filters. Without a bandpass filter, the absolute CH_4 removal was 10.4×10^{-3} CH_4 molecules per $FeCl_3 \cdot 6H_2O$ molecule. (Right) The change in the abundance of ^{13}C is shown as $\Delta\delta^{13}CH_4$. "none" indicates that no bandpass filter was used during the experiment. Steady-state calculations of Cl are shown in Appendix section A6. The error bars represent the standard deviation.

The change in measured methane concentration was used as a proxy for chlorine radical production, as shown in Reaction R17.

$$CH_4 + Cl\cdot \quad \rightleftharpoons \quad CH_3\cdot + HCl \tag{R17}$$

The x-axis in Figure 9 is ordered according to the centre wavelength of the bandpass filter used in the experiments, where "none" indicates that no bandpass filter was used. The spectral irradiance for the bandpass filters is displayed in Figure 4.

The absolute and energy normalized methane removal is shown in Figure 9 (Left) in units of CH_4 molecules per $FeCl_3 \cdot 6H_2O$ molecule. The energy normalization was calculated for the absolute removal at 408 nm and the integrated spectral irradiance for each bandpass filter. As the bandpass filters do not have the same wavelength width or energy throughput, Figure 4, the energy normalization contradicts this effect.

The largest average methane removal occurs at 436 nm. At this wavelength, the removal corresponds to 3.3×10^{-3} and 2.0×10^{-3} CH_4 per $FeCl_3 \cdot 6H_2O$ for absolute and energy normalized removal, respectively. This means that chlorine generation is small relative to the iron chloride reservoir in the sample. The lowest average methane removal occurs at 523 nm, 0.3×10^{-3} and 0.8×10^{-3} CH_4 per $FeCl_3 \cdot 6H_2O$ for absolute and energy normalized removal, respectively.

The reaction of methane with chlorine is highly fractionating, and an increase in $\delta^{13}CH_4$ would suggest that chlorine is the oxidizing agent and not a different oxidation pathway, e.g. hydroxyl radicals. The abundance of ^{13}C in CH_4, measured as $\delta^{13}CH_4$, is measured during the experiments with the Picarro G2201-i, and is shown in Figure 9 (Right) as the change in the delta value.

A chlorine steady-state (Cl SS) concentration was calculated from the observed CH_4 removal (seen in Figure 9 (Left)) to derive the concentration of chlorine required to remove an amount of methane (the Cl SS calculation equations are shown in Appendix section A6). The expected $\delta^{13}CH_4$ was calculated using the SS Cl concentration with the rate constants for the chlorine oxidation of $^{12}CH_4$ and $^{13}CH_4$. The expected $\delta^{13}CH_4$ value is shown in green together with the measured change in the delta value in Figure 9 (Right).

Oxidation of methane by OH radicals results in a fractionation 17 times smaller than for the methane - Cl reaction (Saueressig et al., 2001, 1995). A lower observed than expected change in the delta value would indicate an additional removal pathway with a lower kinetic isotope effect (e.g. OH). The observed and expected $\Delta\delta^{13}CH_4$ values are equal to within the experimental uncertainties, except for the experiment made using the 436 nm bandpass filter, which is just outside the mutual uncertainties; we think this was an anomaly due to a calibration offset. Figure 9 (Right) shows a clear correlation between the expected and the observed $\delta^{13}CH_4$ indicating that chlorine is the oxidizing agent throughout all experiments.

4 Conclusions

In this work, we have presented a detailed description of the photolysis of iron(III) chlorides in aerosols. Modelling, quantum chemical calculations and laboratory experiments have provided crucial insight into how iron(III) chloride chromophores behave in aqueous solutions under varying conditions of pH.

Three AEM scenarios were built to describe the speciation of the iron chlorides and the competition inhibiting their formation from hydroxide, sulphate, and other seawater ions. The results show that iron(III) chlorides are the dominant forms of iron at pH<4.0, and iron(III) hydroxides at pH above this. The addition of sulphate decreased the abundance of $FeCl_2^+$ by up to 40 %. The other seawater species we tested did not have a significant effect. The speciation of $FeCl^{2+}$ and $FeCl_2^+$ changes by up to 70 % over the temperature range of 0 to 100 °C.

Quantum chemical calculations made using the density functional theory method CAM-B3LYP/6-311++G(d,p) were used to investigate $FeCl^{2+}$, $FeCl_2^+$, $FeCl_3$, and $FeCl_4^-$. Solvent effects for vacuum, solid, seawater, and water were included using the PCM model and relative permittivities. The four iron chloride species all showed to absorb light in the visible spectrum, where seawater and water absorptions are virtually identical. Dissociation energy thresholds were found using transition state calculations to evaluate the energy when a chlorine atom leaves the system. For $FeCl^{2+}$, $FeCl_2^+$, and $FeCl_4^-$ inclusion of the

energy threshold significantly decreased the absorption rates. $FeCl_3$ was the only species without sunlight-limiting energy thresholds in any solvent. In water, $FeCl_3$ has the fastest integrated absorption rate of 259 $\times$ 10^{-3} s^{-1} and $FeCl^{2+}$ had the overall slowest rate.

We examined the photolysis of solid $FeCl_3 \cdot 6H_2O$ in nine wavelength intervals using bandpass filters with centre wavelengths ranging from 408 to 601 nm. The maximum methane removal was observed for the 436 nm bandpass filter to be 2.0 $\times$ 10^{-3} CH_4 molecules per $FeCl_3 \cdot 6H_2O$, whereas the removal efficiency without a bandpass filter was 10.4 $\times$ 10^{-3} CH_4 molecules per $FeCl_3 \cdot 6H_2O$ including energy normalization. No statistically significant methane removal was observed at wavelengths longer than 523 nm. The observed $\Delta\delta^{13}CH_4$ concluded that methane is oxidized by chlorine and not OH. Maximum chlorine production was found at an excitation wavelength of around 436 nm.

We conclude that the catalytic efficiency of the iron chloride mechanism will be constrained by several environmental variables. The pH of the system plays an important role, affecting the abundance of the $FeCl_n^{3-n}$ chromophores. Fenton oxidation of Fe(II) to Fe(III) will result in production of base, which is countered by the absorption of environmental acids like HCl, H_2SO_4, HNO_3 and organic acids. The concentration of chloride also impacts the abundance and distribution of the $FeCl_n^{3-n}$ chromophores and will be affected by equilibrium with atmospheric humidity, and the emission and re-absorption of HCl. The presence of anions other than Cl^-, such as sulfate and fluoride, may reduce the availability of Fe(III) for chloride chromophores.

Further research is needed in order to explore the catalytic efficiency of ionic iron and chlorine recycling, under the many different conditions in the troposphere and marine boundary layer, before the iron chloride mechanism can be considered as a potential climate intervention.

Appendix A: Supplementary Methods

A1 Aqueous Equilibrium Model: Species added manually to the Visual MinteQ database

Table A1. Thermodynamic data for species added to the MinteQ models. The values were calculated from data by Tagirov et al. (2000) (Tagirov et al., 2000). Molar weight (M_w), equilibrium constant (log(K)), change in enthalpy (ΔH).

Species	**M_w / (g mol^{-1})**	**log(K)**	**ΔH / (kJ mol^{-1})**
$FeCl^{2+}$	91.3	2.6	43.5
$FeCl_2^+$	126.8	3.9	1.3
$FeCl_3$	162.2	-2.7	146.8

A2 Geometries of iron(III) chlorides

Table A2. Geometries of minima and TS for $FeCl^{2+}$. TS and relative permittivities are given in parentheses. The TS is not optimized if not given otherwise. Lennard-Jones potential. Values given in units of Å.

Atom	X	Y	Z
$FeCl^{2+}$ - Vacuum			
Fe	0.00000000	0.00000000	0.89243200
Cl	0.00000000	0.00000000	-1.36489500
$FeCl^{2+}$ - Vacuum (Optimized LJ Potential)			
Fe	0.00000000	0.00000000	1.36685000
Cl	0.00000000	0.00000000	-2.09047700
$FeCl^{2+}$ - Solid (2.0)			
Fe	0.00000000	0.00000000	0.92908200
Cl	0.00000000	0.00000000	-1.42094900
$FeCl^{2+}$ - Solid (10.0)			
Fe	0.00000000	0.00000000	0.97379200
Cl	0.00000000	0.00000000	-1.48932800
$FeCl^{2+}$ - Water (78.4)			
Fe	0.00000000	0.00000000	0.98773100
Cl	0.00000000	0.00000000	-1.51064700
$FeCl^{2+}$ - Water (Optimized TS, 78.4)			
Fe	0.00000000	0.00000000	1.25047300
Cl	0.00000000	0.00000000	-1.97410000

Table A3. Geometries of minima and TS for $FeCl_2^+$. TS and relative permittivities are given in parentheses. The TS is not optimized if not otherwise indicated. Lennard-Jones potential. Values given in units of Å.

Atom	X	Y	Z
$FeCl_2^+$ - Vacuum			
Fe	0.00000000	0.00000000	0.64324200
Cl	0.00000000	1.67657400	-0.49189100
Cl	0.00000000	-1.67657400	-0.49189100
$FeCl_2^+$ - Vacuum (LJ Potential)			
Fe	0.00000000	-1.14903500	0.00000000
Cl	0.93891500	4.80205800	0.00000000
Cl	-0.93891500	-3.04471000	0.00000000
$FeCl_2^+$ - Solid (2.0)			
Fe	0.00000000	0.00000000	0.77985900
Cl	0.00000000	1.54863200	-0.59636300
Cl	0.00000000	-1.54863200	-0.59636300
$FeCl_2^+$ - Solid (10.0)			
Fe	0.00000000	0.00000000	0.82053800
Cl	0.00000000	1.50744300	-0.62747000
Cl	0.00000000	-1.50744300	-0.62747000
$FeCl_2^+$ - Water (78.4)			
Fe	0.00000000	0.00000000	0.82832900
Cl	0.00000000	1.51047300	-0.63342800
Cl	0.00000000	-1.51047300	-0.63342800
$FeCl_2^+$ - Water (LJ Potential, 78.4)			
Fe	0.00000000	-1.53061900	0.00000000
Cl	1.53198900	2.27452700	0.00000000
Cl	-1.53198900	0.06642000	0.00000000

Table A4. Geometries of minima and TS for $FeCl_3$. TS and relative permittivities are given in parentheses. The TS is not optimized if not otherwise indicated. Values given in units of Å.

Atom	X	Y	Z
$FeCl_3$ - Vacuum			
Fe	0.00000000	0.00000000	0.06229900
Cl	0.00000000	0.00000000	2.12724600
Cl	0.00000000	1.70272000	-1.11126300
Cl	0.00000000	-1.70272000	-1.11126300
$FeCl_3$ - Vacuum (Optimized TS)			
Fe	0.00000000	0.19936900	0.00000000
Cl	-0.23316300	2.26248200	0.00000000
Cl	-1.59583200	-1.78955500	0.00000000
Cl	1.82899600	-0.77784400	0.00000000
$FeCl_3$ - Solid (2.0)			
Fe	0.00000000	0.00000000	0.09462900
Cl	0.00000000	0.00000000	2.17353500
Cl	0.00000000	1.66523400	-1.15913100
Cl	0.00000000	-1.66523400	-1.15913100
$FeCl_3$ - Solid (10.0)			
Fe	0.00000000	0.00000000	0.16164100
Cl	0.00000000	0.00000000	2.27392600
Cl	0.00000000	1.58394800	-1.26057100
Cl	0.00000000	-1.58394800	-1.26057100
$FeCl_3$ - Water (78.4)			
Fe	0.00000000	0.00000000	0.17565400
Cl	0.00000000	0.00000000	2.30557800
Cl	0.00000000	1.57451400	-1.28711300
Cl	0.00000000	-1.57451400	-1.28711300
$FeCl_3$ - Water (Optimized TS, 78.4)			
Fe	0.26266300	0.28139600	-0.18588400
Cl	2.45315100	0.14460200	0.13374700
Cl	-1.91616200	1.03074500	0.11469600
Cl	-0.93871000	-1.60571700	0.03584900

Table A5. Geometries of minima and TS for $FeCl_4^-$. TS and relative permittivities are given in parentheses. The TS is not optimized if not otherwise indicated. Values given in units of Å.

Atom	X	Y	Z
	$FeCl_4^-$ - Vacuum		
Fe	0.0150980	0.0027010	0.0786570
Cl	-1.8497650	-0.0129990	1.2143290
Cl	-0.2089620	-1.6349200	-1.3253390
Cl	0.0482380	1.8732870	-1.0241150
Cl	1.9873980	-0.2295000	1.0148250
	$FeCl_4^-$ - Vacuum (TS)		
Fe	-0.3705550	0.0003460	-0.0214210
Cl	3.5129100	-0.0002720	-0.0031090
Cl	-0.9707510	-0.0127400	2.0163570
Cl	-0.9874020	1.7870870	-0.9795580
Cl	-0.9880270	-1.7746060	-1.0009290
	$FeCl_4^-$ - Solid (2.0)		
Fe	-0.0121400	-0.0032990	0.0983290
Cl	0.1515470	1.6578120	-1.2840190
Cl	-1.9913620	0.1824750	1.0231410
Cl	-0.0442120	-1.8511330	-1.0394650
Cl	1.9025950	0.0158910	1.1499570
	$FeCl_4^-$ - Solid (10.0)		
Fe	-0.0039350	-0.0073460	-0.1784210
Cl	2.0378400	0.0695040	-0.9607470
Cl	0.0120240	-1.8310140	1.0092500
Cl	0.0139720	1.7030320	1.1614890
Cl	-2.0578180	0.0697140	-0.9371140
	$FeCl_4^-$ - Water (78.4)		
Fe	-0.0006960	-0.0067460	-0.2094960
Cl	2.0784560	0.0677370	-0.8820680
Cl	0.0065630	-1.8373510	0.9761920
Cl	-0.0033190	1.7208020	1.1060030
Cl	-2.0806360	0.0591290	-0.8797220
	$FeCl_4^-$ - Water (TS, 78.4)		
Fe	-0.3705550	0.0003460	-0.0214210
Cl	3.5129100	-0.0002720	-0.0031090
Cl	-0.9707510	-0.0127400	2.0163570
Cl	-0.9874020	1.7870870	-0.9795580
Cl	-0.9880270	-1.7746060	-1.0009290

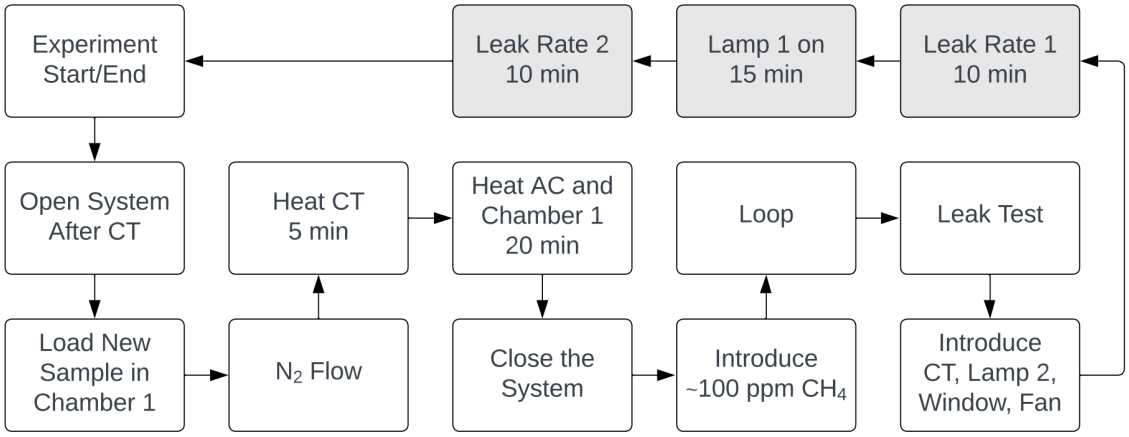

Figure A1. Overview of the experimental procedure. Data is retrieved during the three grey highlighted steps. Abbreviations: Cold Trap (CT), Active Carbon Trap (AC), different bandpass filters.

A3 Experimental Procedure

When the experimental procedure begins, the system is opened between the active carbon trap and the two measuring instruments. While the system is open, the flow is increased, and an overpressure vent is closed to flush the system. A $FeCl_3 \cdot 6H_2O$ sample of 20 mg is now measured in a 10 mL beaker on a fine scale. The Sample Chamber is cleaned with Milli-Q water on some paper and wiped again with dry paper. The beaker is placed in the Sample Chamber, and the chamber is closed. Two O-rings ensure a tight closure of the Sample Chamber. While the system is open, the cold trap is heated for 5 minutes to flush condensed species out of the system. The active carbon trap is heated for 20 minutes to release the captured CO_2. The Sample Chamber is heated simultaneously with the active carbon trap to minimize the temperature difference in the Sample Chamber when the xenon lamp is turned on. After the heating processes, the flow is decreased by opening the over-pressure vent, and the system is closed. There is now flow through the whole system. During the process of closing the system, the CO_2 and H_2O concentrations are recorded by the Picarro to ensure that the active carbon trap works properly. Methane is now introduced with a syringe to the nitrogen flow. The methane concentration in the system rises to 200 to 400 ppm, and the four-port valve is closed at around 150 ppm. Initiating the methane is controlled live with the Axetris instrument. After the looping process is started the methane concentration is monitored to ensure it stabilizes at around 95 ppm. After approximately five minutes, the stability test begins. Due to a small underpressure in the system, the presence of a possible leak is quantified by spraying pure methane from a syringe at joints, seals and so on, and observing whether the methane concentration in the system increases. After the system has passed the stability test the cold trap, bandpass filter, fan, and the UV-LED are initiated. The two instruments are both slightly sensitive to temperature, 'leak rate 1' is therefore initiated five minutes after the cold trap is introduced, to measure stability. The next step is recording the leak rate over 10 minutes before illumination. The xenon lamp is turned on for exactly 15 minutes, and the second leak rate is measured over the following 10 minutes. One experiment has now ended,

and the procedure is repeated with a new sample of $FeCl_3 \cdot 6H_2O$. The different bandpass filters and light sources are discussed in methods (Section 2.3). Each of the 10 bandpass filters was used for three experiments.

A4 Light sources used in the experiments

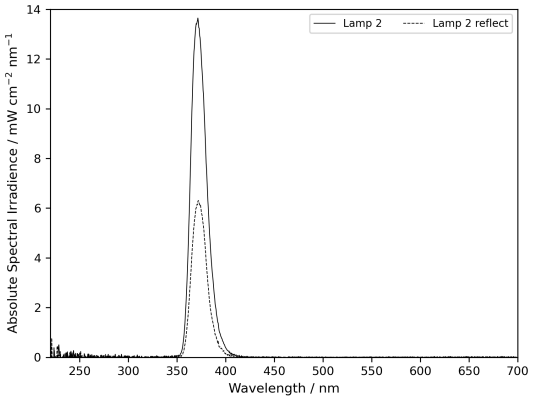

Figure A2. Light source spectra. The UV-LED was a Luminus SST-10-UV Surface-Mount LED lamp. The spectrum is recorded by an Ocean Optics Flame-S Miniature UV-Vis-NIR spectrometer, and a fibre optic cable with a diameter of 600 μm before and after the chamber.

The xenon lamp, bandpass filters, and sample chamber were placed according to the experimental setup when the irradiance was measured. The chamber setup with measurements can be seen in Figure A3. The Ocean Optics spectrometer was placed at a distance according to the bottom of the chamber, to estimate the light exposure for the sample. A calibration was used for the Ocean Optics spectrometer using the standard manual and light source from Ocean Optics (DH-2000, UV-Vis-NIR calibration light source). The irradiance of the UV-LED is shown in Figure A2.

A5 The Sample Chamber setup and measurements

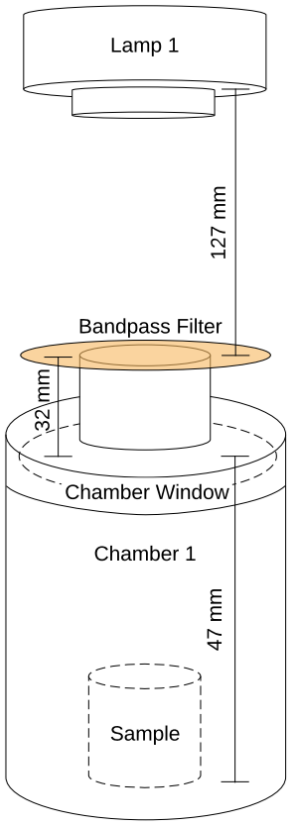

Figure A3. Measurements of the Sample Chamber setup during the experiments, including the Ocean Optics spectrometer analysis. The Sample Chamber had a volume of 0.36 L.

A6 Calculation of Steady State chlorine atom concentration and nominal $\delta^{13}CH_4$

The steady-state concentration of chlorine atoms is calculated with the assumption of a constant source and sink of chlorine. The decay of methane can be described as a pseudo-first-order reaction, in Equation A1:

$$CH_4(t) = CH_4(0) \times e^{-rt} \tag{A1}$$

Where t is the time and r is the first order loss rate in Equation A2. $k(^{12}CH_4)$ is the rate constant of the $^{12}CH_4$ + Cl reaction, and $[Cl]_{ss}$ is the chlorine concentration.

$$r = k(^{12}CH_4) \times [Cl]_{ss} \tag{A2}$$

The Cl SS concentration is isolated and used to calculate the expected isotope shift. The kinetic isotope effect α is used to define the isotopic fractionation ϵ (Johnson et al., 2002):

$$\alpha = \frac{k(^{12}CH_4)}{k(^{13}CH_4)} \tag{A3}$$

$$\epsilon = \alpha - 1 \tag{A4}$$

The final isotopic enrichment δ is calculated based on the enrichment of the starting material δ_0, ϵ, and the extent of reaction, f:

$$\delta = \delta_0 + \epsilon \cdot ln(f) \tag{A5}$$

Appendix B: Supplementary Results

B1 Ab Initio Calculations: $FeCl_3$

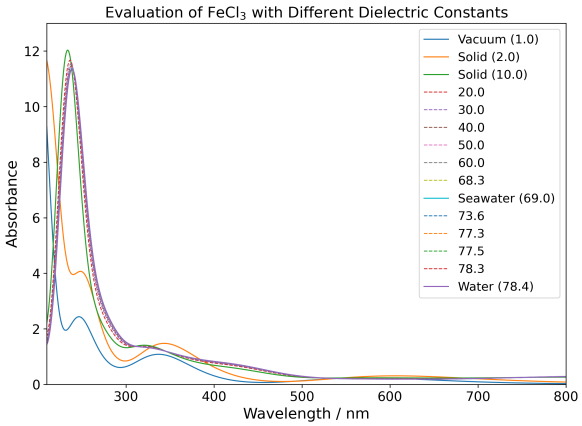

Figure B1. Absorption of $FeCl_3$ calculated with CAM-B3LYP/6-311++G(d,p). Solid (2.0) and solid (10.0) are estimated to represent the optic and static relative permittivity for the solid state of $FeCl_3$, respectively.

B2 All Aqueous Equilibrium Models

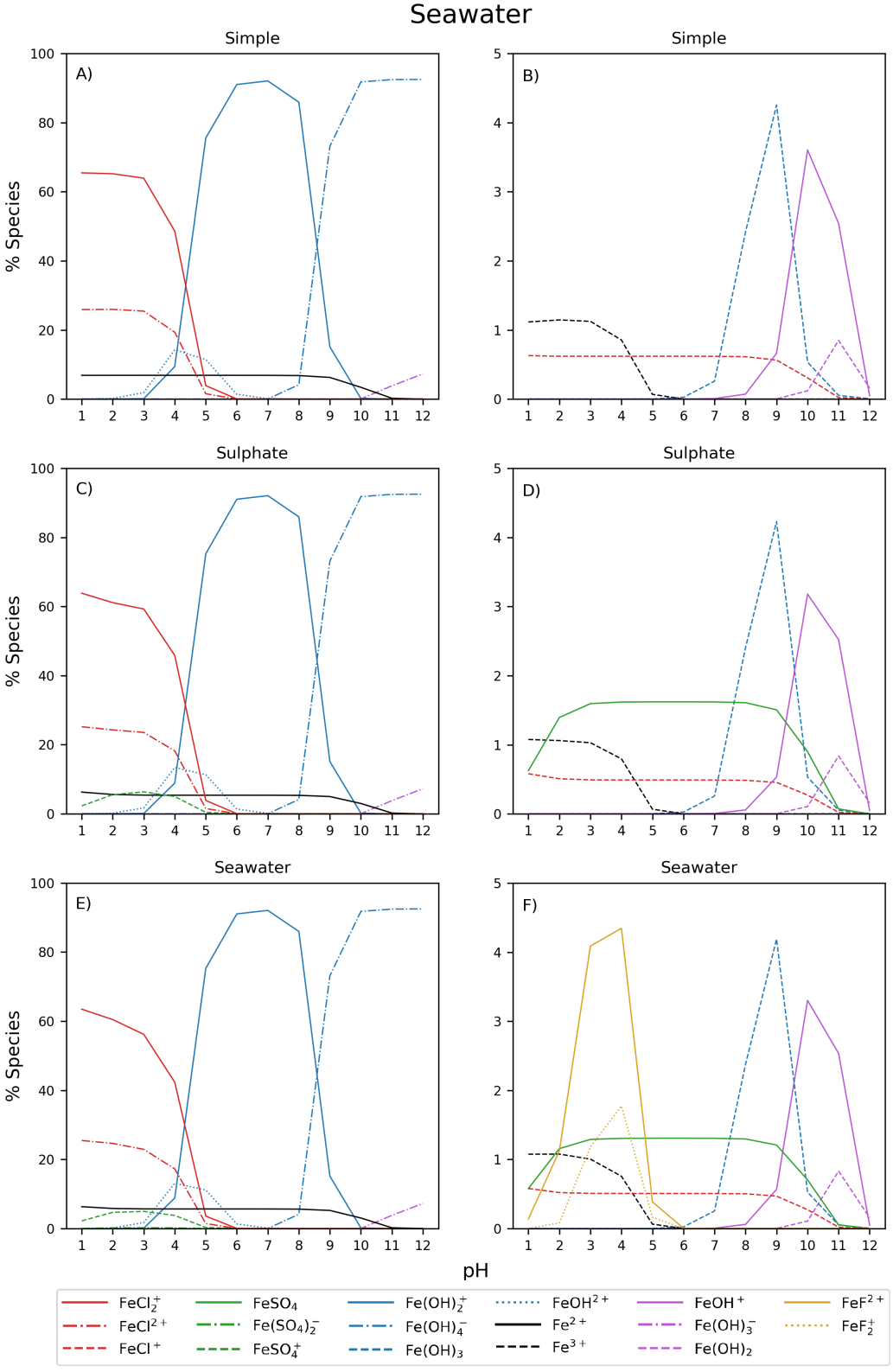

Figure B2. Simple, Sulphate and Seawater Aqueous Equilibrium Models with a total iron concentration of 9.76×10^{-13} mol/kg (Fe_S). The right column is zoomed in from 0 to 5 %.

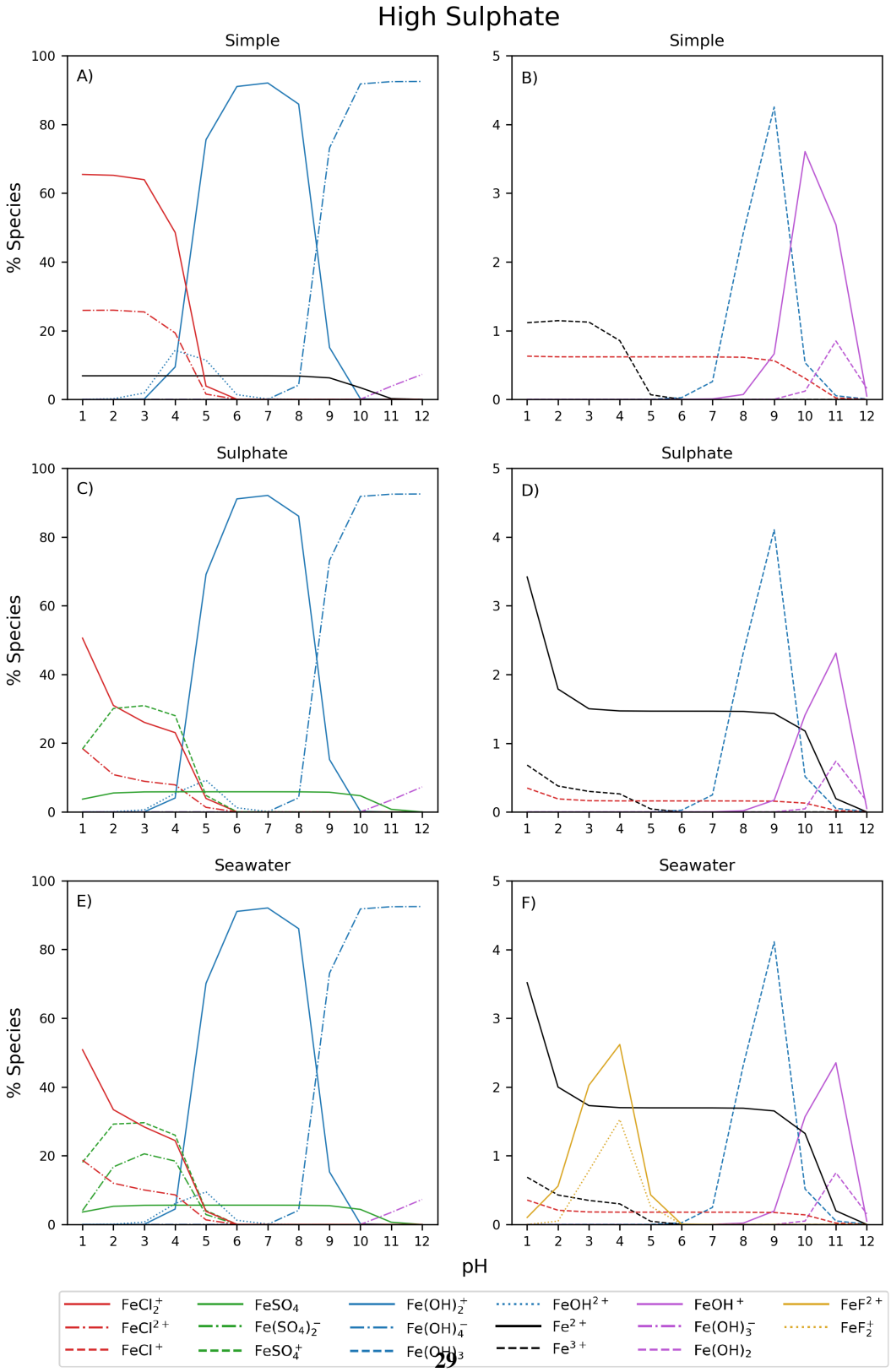

Figure B3. Simple, Sulphate and Seawater Aqueous Equilibrium Models with a 10 times higher sulphate concentration (2.82×10^{-1} mol/kg)

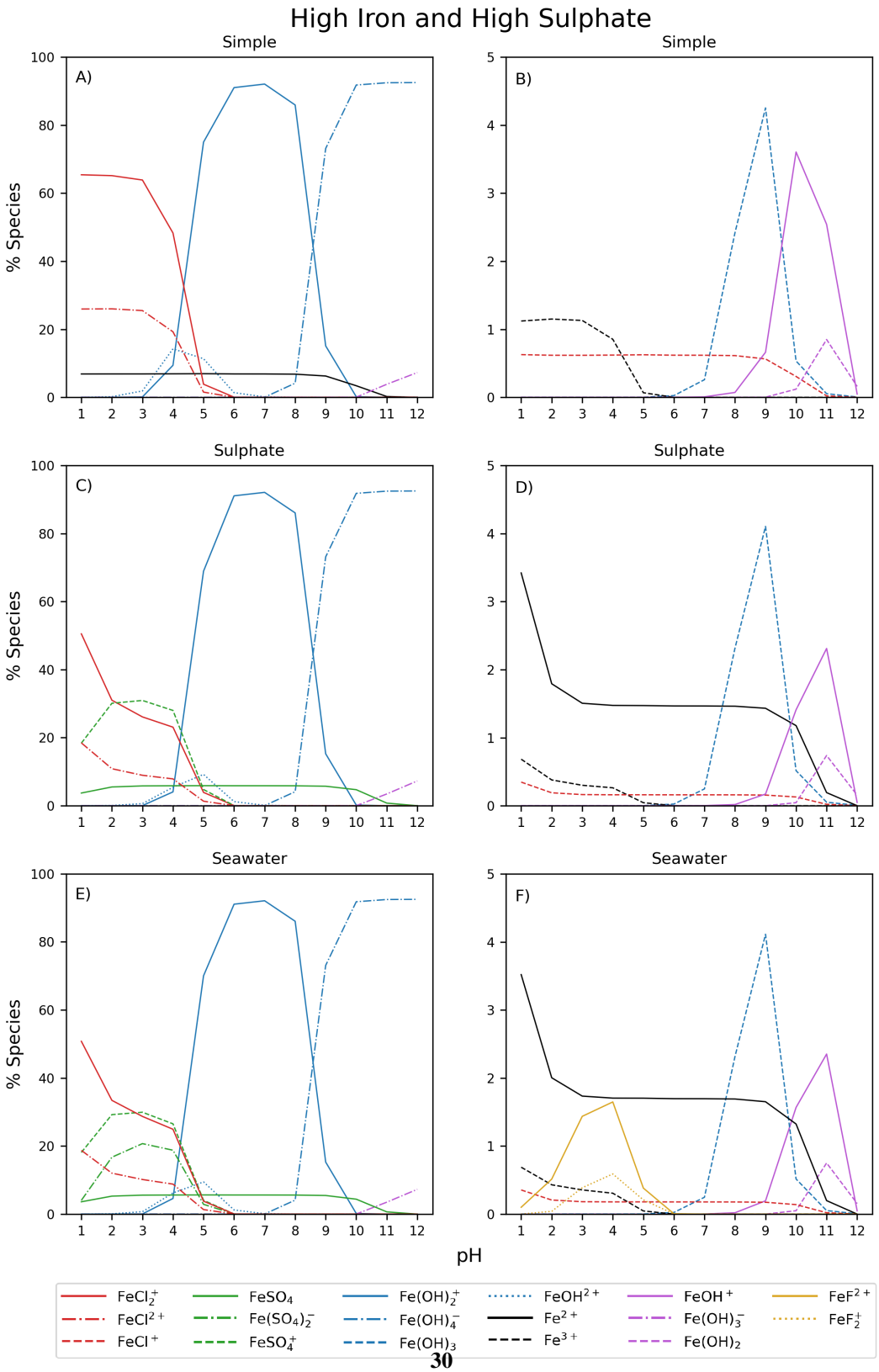

Figure B4. Simple, Sulphate and Seawater Aqueous Equilibrium Models with a total iron concentration of 9.17×10^{-4} mol/kg (Fe_A). The

Data availability. Contact Matthew S. Johnson, msj@chem.ku.dk, for available data sets.

Author contributions. MKM, MvH and MSJ designed the research. MKM and JBL prepared the laboratory experiments with advise from MvH and MSJ. MKM performed and analysed the quantum chemistry calculations, modelling results, and laboratory experiments. JBL helped with the laboratory experiments and the data analysis was carried out by MKM with input from JBL, MSJ and MvH. KVM contributed to the design and support of the quantum chemistry calculations and interpretation of the results. MKM and MSJ wrote the paper. All authors edited and approved the manuscript.

Competing interests. The University of Copenhagen (UCPH) has filed a patent application related to atmospheric iron chlorides on behalf of its inventors (MvH, MSJ). All other authors declare they have no competing interests.

Acknowledgements. We thank Spark Climate Solutions for supporting this research as a part of the ISAMO project. Thanks to everyone on the ISAMO project for helpful comments and discussions. We also thank Jacob Lynge Elholm for assistance with the ab initio calculations.

References

Abou-Ghanem, M., Oliynyk, A. O., Chen, Z., Matchett, L. C., McGrath, D. T., Katz, M. J., Locock, A. J., and Styler, S. A.: Significant variability in the photocatalytic activity of natural titanium-containing minerals: implications for understanding and predicting atmospheric mineral dust photochemistry, Environmental Science & Technology, 54, 13 509–13 516, 2020.

Achterberg, E. P., Holland, T. W., Bowie, A. R., Mantoura, R. F. C., and Worsfold, P. J.: Determination of iron in seawater, Analytica Chimica Acta, 442, 1–14, 2001.

Allan, W., Struthers, H., and Lowe, D.: Methane carbon isotope effects caused by atomic chlorine in the marine boundary layer: Global model results compared with Southern Hemisphere measurements, Journal of Geophysical Research: Atmospheres, 112, 2007.

Angle, K. J., Crocker, D. R., Simpson, R. M., Mayer, K. J., Garofalo, L. A., Moore, A. N., Mora Garcia, S. L., Or, V. W., Srinivasan, S., Farhan, M., et al.: Acidity across the interface from the ocean surface to sea spray aerosol, Proceedings of the National Academy of Sciences, 118, e2018397 118, 2021.

Badia, A., Reeves, C. E., Baker, A. R., Saiz-Lopez, A., Volkamer, R., Koenig, T. K., Apel, E. C., Hornbrook, R. S., Carpenter, L. J., Andrews, S. J., et al.: Importance of reactive halogens in the tropical marine atmosphere: a regional modelling study using WRF-Chem, Atmospheric Chemistry and Physics, 19, 3161–3189, 2019.

Cantrell, C. A., Shetter, R. E., McDaniel, A. H., Calvert, J. G., Davidson, J. A., Lowe, D. C., Tyler, S. C., Cicerone, R. J., and Greenberg, J. P.: Carbon kinetic isotope effect in the oxidation of methane by the hydroxyl radical, Journal of Geophysical Research: Atmospheres, 95, 22 455–22 462, 1990.

Chang, S. and Allen, D. T.: Atmospheric chlorine chemistry in southeast Texas: Impacts on ozone formation and control, Environmental science & technology, 40, 251–262, 2006.

Chen, H., Nanayakkara, C. E., and Grassian, V. H.: Titanium dioxide photocatalysis in atmospheric chemistry, Chemical reviews, 112, 5919–5948, 2012.

Fenton, H. J. H.: Oxidation of tartaric acid in presence of iron, Journal of the Chemical Society, Transactions, 65, 899–910, 1894.

Francl, M. M., Pietro, W. J., Hehre, W. J., Binkley, J. S., Gordon, M. S., DeFrees, D. J., and Pople, J. A.: Self-consistent molecular orbital methods. XXIII. A polarization-type basis set for second-row elements, The Journal of Chemical Physics, 77, 3654–3665, 1982.

Frisch, M. J., Trucks, G. W., Schlegel, H. B., Scuseria, G. E., Robb, M. A., Cheeseman, J. R., Scalmani, G., Barone, V., Petersson, G. A., Nakatsuji, H., Li, X., Caricato, M., Marenich, A. V., Bloino, J., Janesko, B. G., Gomperts, R., Mennucci, B., Hratchian, H. P., Ortiz, J. V., Izmaylov, A. F., Sonnenberg, J. L., Williams-Young, D., Ding, F., Lipparini, F., Egidi, F., Goings, J., Peng, B., Petrone, A., Henderson, T., Ranasinghe, D., Zakrzewski, V. G., Gao, J., Rega, N., Zheng, G., Liang, W., Hada, M., Ehara, M., Toyota, K., Fukuda, R., Hasegawa, J., Ishida, M., Nakajima, T., Honda, Y., Kitao, O., Nakai, H., Vreven, T., Throssell, K., Montgomery, Jr., J. A., Peralta, J. E., Ogliaro, F., Bearpark, M. J., Heyd, J. J., Brothers, E. N., Kudin, K. N., Staroverov, V. N., Keith, T. A., Kobayashi, R., Normand, J., Raghavachari, K., Rendell, A. P., Burant, J. C., Iyengar, S. S., Tomasi, J., Cossi, M., Millam, J. M., Klene, M., Adamo, C., Cammi, R., Ochterski, J. W., Martin, R. L., Morokuma, K., Farkas, O., Foresman, J. B., and Fox, D. J.: Gaussian~16 Revision C.01, gaussian Inc. Wallingford CT, 2016.

Gamlen, G. and Jordan, D.: 295. A spectrophotometric study of the iron (III) chloro-complexes, Journal of the Chemical Society (Resumed), pp. 1435–1443, 1953.

Gromov, S., Brenninkmeijer, C. A., and Jöckel, P.: A very limited role of tropospheric chlorine as a sink of the greenhouse gas methane, Atmospheric Chemistry and Physics, 18, 9831–9843, 2018.

Harnung, S. E. and Johnson, M. S.: Chemistry and the Environment, Cambridge University Press, 2012.

Hossaini, R., Chipperfield, M. P., Saiz-Lopez, A., Fernandez, R., Monks, S., Feng, W., Brauer, P., and Von Glasow, R.: A global model of tropospheric chlorine chemistry: Organic versus inorganic sources and impact on methane oxidation, Journal of Geophysical Research: Atmospheres, 121, 14–271, 2016.

Hsu, S.-C., Liu, S. C., Arimoto, R., Shiah, F.-K., Gong, G.-C., Huang, Y.-T., Kao, S.-J., Chen, J.-P., Lin, F.-J., Lin, C.-Y., et al.: Effects of acidic processing, transport history, and dust and sea salt loadings on the dissolution of iron from Asian dust, Journal of Geophysical Research: Atmospheres, 115, 2010.

J. P. Gustafsson: Visual MINTEQ ver. 3.1 [software], https://vminteq.lwr.kth.se/, (released 2014).

Johnson, M., Feilberg, K., von Hessberg, P., and Nielsen, O.: Isotopic processes in atmospheric chemistry, Chemical Society Reviews, 31, 313–323, 2002.

Knipping, E. M. and Dabdub, D.: Impact of chlorine emissions from sea-salt aerosol on coastal urban ozone, Environmental science & technology, 37, 275–284, 2003.

Korte, D., Bruzzoniti, M. C., Sarzanini, C., and Franko, M.: Influence of foreign ions on determination of ionic Ag in water by formation of nanoparticles in a FIA-TLS system, Analytical letters, 44, 2901–2910, 2011.

Lawler, M., Sander, R., Carpenter, L., Lee, J., Von Glasow, R., Sommariva, R., and Saltzman, E.: HOCl and Cl 2 observations in marine air, Atmospheric Chemistry and Physics, 11, 7617–7628, 2011.

Li, Q., Fernandez, R. P., Hossaini, R., Iglesias-Suarez, F., Cuevas, C. A., Apel, E. C., Kinnison, D. E., Lamarque, J.-F., and Saiz-Lopez, A.: Reactive halogens increase the global methane lifetime and radiative forcing in the 21st century, Nature Communications, 13, 2768, 2022.

Li, Q., Meidan, D., Hess, P., Añel, J. A., Cuevas, C. A., Doney, S., Fernandez, R. P., van Herpen, M., Höglund-Isaksson, L., Johnson, M. S., and et al.: Global environmental implications of atmospheric methane removal through chlorine-mediated chemistry-climate interactions, Nat Commun, 14, 2023.

Lindén, L., Rabek, J., Kaczmarek, H., Kaminska, A., and Scoponi, M.: Photooxidative degradation of polymers by HOxxx and HO2xxx radicals generated during the photolysis of H2O2, FeCl3, and Fenton reagents, Coordination chemistry reviews, 125, 195–217, 1993.

Loures, C. C., Alcântara, M. A., Izário Filho, H. J., Teixeira, A., Silva, F. T., Paiva, T. C., and Samanamud, G.: Advanced oxidative degradation processes: fundamentals and applications, International Review of Chemical Engineering, 5, 102–120, 2013.

Madronich, S., Flocke, S., Zeng, J., Petropavlovskikh, I., and Lee-Taylor, J.: Tropospheric ultraviolet and visible (TUV) radiation model, 2002.

Mak, J. E., Kra, G., Sandomenico, T., and Bergamaschi, P.: The seasonally varying isotopic composition of the sources of carbon monoxide at Barbados, West Indies, Journal of Geophysical Research: Atmospheres, 108, 2003.

Maric, D., Burrows, J., Meller, R., and Moortgat, G.: A study of the UV—visible absorption spectrum of molecular chlorine, Journal of Photochemistry and Photobiology A: Chemistry, 70, 205–214, 1993.

McLean, A. and Chandler, G.: Contracted Gaussian basis sets for molecular calculations. I. Second row atoms, Z= 11–18, The Journal of Chemical Physics, 72, 5639–5648, 1980.

Meyer-Oeste, F. D.: Troposphere cooling procedure, 2014.

Midi, N. S., Sasaki, K., Ohyama, R.-i., and Shinyashiki, N.: Broadband complex dielectric constants of water and sodium chloride aqueous solutions with different DC conductivities, IEEJ Transactions on Electrical and Electronic Engineering, 9, S8–S12, 2014.

Nadtochenko, V. A. and Kiwi, J.: Photolysis of FeOH2+ and FeCl2+ in aqueous solution. Photodissociation kinetics and quantum yields, Inorganic Chemistry, 37, 5233–5238, 1998.

Nielsen, L. S. and Bilde, M.: Exploring controlling factors for sea spray aerosol production: temperature, inorganic ions and organic surfactants, Tellus B: Chemical and Physical Meteorology, 72, 1–10, 2020.

Oeste, F. D.: Ferrous aerosol emission method for self-releasing cooling of atmosphere, involves adding compound of iron and/or bromine and/or chlorine to solid fuel and/or gas fuel and mixing flue gases of solid fuel and/or gas fuel, Bundesrepublik Deutschland Deutsches Patent- und Markenamt DE102009004281A,, 2009.

Ponczek, M. and George, C.: Kinetics and product formation during the photooxidation of butanol on atmospheric mineral dust, Environmental science & technology, 52, 5191–5198, 2018.

Read, K., Lee, J., Lewis, A., Moller, S., Mendes, L., and Carpenter, L.: Intra-annual cycles of NMVOC in the tropical marine boundary layer and their use for interpreting seasonal variability in CO, Journal of Geophysical Research: Atmospheres, 114, 2009.

Saiz-Lopez, A. and von Glasow, R.: Reactive halogen chemistry in the troposphere, Chem. Soc. Rev., 41, 6448–6472, https://doi.org/10.1039/C2CS35208G, 2012.

Saueressig, G., Bergamaschi, P., Crowley, J., Fischer, H., and Harris, G.: Carbon kinetic isotope effect in the reaction of CH4 with Cl atoms, Geophysical Research Letters, 22, 1225–1228, 1995.

Saueressig, G., Crowley, J. N., Bergamaschi, P., Brühl, C., Brenninkmeijer, C. A., and Fischer, H.: Carbon 13 and D kinetic isotope effects in the reactions of CH4 with O (1 D) and OH: new laboratory measurements and their implications for the isotopic composition of stratospheric methane, Journal of Geophysical Research: Atmospheres, 106, 23 127–23 138, 2001.

Seinfeld, J. and Pandis, S.: Atmospheric chemistry and physics. 1997, New York, 2008.

Sherwen, T., Schmidt, J. A., Evans, M. J., Carpenter, L. J., Großmann, K., Eastham, S. D., Jacob, D. J., Dix, B., Koenig, T. K., Sinreich, R., et al.: Global impacts of tropospheric halogens (Cl, Br, I) on oxidants and composition in GEOS-Chem, Atmospheric Chemistry and Physics, 16, 12 239–12 271, 2016.

Simpson, W. R., Brown, S. S., Saiz-Lopez, A., Thornton, J. A., and von Glasow, R.: Tropospheric Halogen Chemistry: Sources, Cycling, and Impacts, Chemical Reviews, 115, 4035–4062, https://doi.org/10.1021/cr5006638, pMID: 25763598, 2015.

Spitznagel, G. W., Clark, T., von Ragué Schleyer, P., and Hehre, W. J.: An evaluation of the performance of diffuse function-augmented basis sets for second row elements, Na-Cl, Journal of Computational Chemistry, 8, 1109–1116, 1987.

Stumm, W. and Morgan, J. J.: Aquatic chemistry: chemical equilibria and rates in natural waters, John Wiley & Sons, 2012.

Tagirov, B. R., Diakonov, I. I., Devina, O. A., and Zotov, A. V.: Standard ferric–ferrous potential and stability of $FeCl^{2+}$ to 90°C. Thermodynamic properties of ${Fe_{(aq)}}^{3+}$ and ferric-chloride species, Chemical Geology, 162, 193–219, 2000.

Tomasi, J., Mennucci, B., and Cancès, E.: The IEF version of the PCM solvation method: an overview of a new method addressed to study molecular solutes at the QM ab initio level, Journal of Molecular Structure; THEOCHEM, 464, 211–226, https://doi.org/10.1016/S0166-1280(98)00553-3, 1999.

Uchikoshi, M., Akiyama, D., Kimijima, K., and Shinoda, K.: The Distribution and Structures of Ferric Aqua and Chloro Complexes in Hydrochloric Acid Solutions, Isij International, 62, 912–921, 2022.

van Herpen, M. M., Li, Q., Saiz-Lopez, A., Liisberg, J. B., Röckmann, T., Cuevas, C. A., Fernandez, R. P., Mak, J. E., Mahowald, N. M., Hess, P., et al.: Photocatalytic chlorine atom production on mineral dust–sea spray aerosols over the North Atlantic, Proceedings of the National Academy of Sciences, 120, e2303974 120, 2023.

Wang, X., Jacob, D. J., Eastham, S. D., Sulprizio, M. P., Zhu, L., Chen, Q., Alexander, B., Sherwen, T., Evans, M. J., Lee, B. H., et al.: The role of chlorine in global tropospheric chemistry, Atmospheric Chemistry and Physics, 19, 3981–4003, 2019.

Wittmer, J. and Zetzsch, C.: Photochemical activation of chlorine by iron-oxide aerosol, Journal of Atmospheric Chemistry, 74, 187–204, 2017.

Wittmer, J., Bleicher, S., and Zetzsch, C.: Iron (III)-induced activation of chloride and bromide from modeled salt pans, The Journal of Physical Chemistry A, 119, 4373–4385, 2015.

Wittmer, J., Bleicher, S., and Zetzsch, C.: Report on the photochemical induced halogen activation of Fe-containing aerosols, J. Climatol. Weather Forecast, 4, 10–4172, 2016.

Yanai, T., Tew, D. P., and Handy, N. C.: A new hybrid exchange–correlation functional using the Coulomb-attenuating method (CAM-B3LYP), Chemical Physics Letters, 393, 51–57, 2004.

Young, C., Washenfelder, R., Edwards, P., Parrish, D., Gilman, J., Kuster, W., Mielke, L., Osthoff, H., Tsai, C., Pikelnaya, O., et al.: Chlorine as a primary radical: evaluation of methods to understand its role in initiation of oxidative cycles, Atmospheric chemistry and physics, 14, 3427–3440, 2014.

Zhu, X., Prospero, J. M., Savoie, D. L., Millero, F. J., Zika, R. G., and Saltzman, E. S.: Photoreduction of iron (III) in marine mineral aerosol solutions, Journal of Geophysical Research: Atmospheres, 98, 9039–9046, 1993.